Journal of Catalysis 278 (2011) 189–199

Contents lists available at ScienceDirect

Journal of Catalysis

journal homepage: www.elsevier.com/locate/jcat

Supported mesoporous solid base catalysts for condensation of carboxylic acids

Ambareesh D. Murkute [a], James E. Jackson [b], Dennis J. Miller [a,*]

[a] Department of Chemical Engineering and Materials Science, Michigan State University, East Lansing, MI 48824, United States
[b] Department of Chemistry, Michigan State University, East Lansing, MI 48824, United States

ARTICLE INFO

Article history:
Received 24 September 2010
Revised 30 November 2010
Accepted 3 December 2010
Available online 20 January 2011

Keywords:
Mesoporous silica
Cerium
Manganese
Ketonization
Carboxylic acids

ABSTRACT

New mesoporous base catalysts (CM-HMS and CM-MCM-41) were synthesized by generating uniform particles of cerium and manganese oxides (MnO_x/CeO_2) *in situ* within hexagonal mesoporous silica (HMS) and MCM-41 supports. These catalysts were characterized by N_2 adsorption, X-ray diffraction (XRD), transmission electron microscopy (TEM), energy-dispersive X-ray spectrometry (EDX), FTIR, temperature-programmed desorption of CO_2 (CO_2-TPD), and diffuse reflectance UV–visible (UV–vis) spectroscopy. Spectroscopic studies reveal that some particles of MnO_x/CeO_2 are incorporated into the walls of the silica network of HMS and MCM-41, while others are highly dispersed onto the surface of the HMS or MCM-41. The catalytic activity of CM-HMS and CM-MCM-41 for the ketonization of carboxylic acids was confirmed; better utilization of Ce and Mn was observed than in unsupported MnO_x/CeO_2. The citrate-based preparation of MnO_x/CeO_2 catalyst supported on HMS and MCM-41 has not been previously reported in the literature.

1. Introduction

Organic acids produced by the fermentation of sugars, starches, or hydrolyzed cellulosic materials constitute a major class of renewable-resource feedstocks that can replace traditional petroleum-derived materials. The condensation of carboxylic acids to ketones, known as ketonization, has long been known; these ketones have potential use as high-energy-density biofuel components and as renewable commodity and specialty chemical building blocks. In the ketonization reaction, two molecules of carboxylic acid condense to form a symmetric ketone, with carbon dioxide and water produced as coproducts. Ketonization is a green and atom-economical process because non-polluting by-products are formed and no solvent or other elaborate reagents are necessary.

The dry distillation of calcium and thorium acetates to yield acetone was reported as early as 1858 [1]; until World War I [2], this reaction was the primary commercial route to acetone. In 1895, Squibb [3] reported the direct ketonization of acetic acid over solid catalysts under flow conditions. Since then, ketonization has been demonstrated over oxide catalysts such as Cr_2O_3 [4,5], Al_2O_3 [6,7], PbO_2 [7], TiO_2 [8–11], ZrO_2 [9,12–14], CeO_2 [14–19], FeO_x [9,10], MnO_2 [7,14,15,17], and Mg/Al hydrotalcites [20], either as bulk materials or supported on pumice, alumina, silica, titania or active carbon. Gliński et al. [15] reported that CeO_2, MnO_2, CdO, and La_2O_3 on SiO_2 were the most active among 20 oxides for the synthesis of acetone from acetic acid. Nagashima et al. [21] modified CeO_2 with metal oxides of Mg, Al, Mn, Fe, Ni, Cu, and Zr and reported that MnO_2/CeO_2 was most effective for ketonization of propionic acid.

The catalytic activity of MnO_x/CeO_2 catalysts is strongly influenced by the preparation method. For example, MnO_x/CeO_2 prepared by conventional co-precipitation is subject to phase segregation and thus exhibits poor ketonization activity [21]. In contrast, evaporation of a solution containing nitrates of cerium and manganese and citric acid, noted here as the citrate process, is considered more effective for preparation of MnO_x/CeO_2 because a uniform precursor is obtained that gives a uniform solid solution of MnO_x/CeO_2 upon calcination. This uniform solid solution is thought to be responsible for the superior activity of MnO_x/CeO_2 prepared by this method, although this bulk MnO_x/CeO_2 has a low surface area (40–50 $m^2\,g^{-1}$). Also, during preparation, an explosive mixture of unreacted citric acid and nitrates of cerium and manganese is formed, which hampers potential for large-scale applications.

The incorporation of the transition and non-transition metals into the silica network of mesoporous materials (MCM-41, HMS) has been reported [22]. However, it is difficult to incorporate Ce into the framework of microporous silicate molecular sieves because the size incompatibility of Ce^{+4} and Si^{4+} ions produces longer (—Si—O—Ce—) bonds and causes high bond-angle strain in the Ce-substituted silica network. In contrast, the substitution of Ce^{4+} into the framework of MCM-41 and HMS is expected to be easy because of the flexibility of mesoporous silica materials [23]. Several authors [23–30] have prepared Ce-MCM-41 catalysts by hydro-

---

* Corresponding author. Fax: +1 517 432 1105.
E-mail address: millerd@egr.msu.edu (D.J. Miller).

0021-9517/$ - see front matter © 2010 Elsevier Inc. All rights reserved.
doi:10.1016/j.jcat.2010.12.001

Nomenclature

a_0	unit cell parameter
BA	butyric acid
C_0	initial concentration of acid (kmol/m^3)
C_T	basic site concentration in the catalyst (kmol/kg cat)
D_{eff}	effective diffusivity
D_p	catalyst support particle diameter
d_{100}	spacing between the 100 planes in the atomic lattice
FWHM	full width of the diffraction peak (degrees) at half maximum
k	rate constant (m^6/kmol/kg cat/s)
n	integer in eq. (7)
PA	propionic acid
$-r_i$	rate of formation of species i (kmol i/m^3/s)
$-r_{i,o}$	rate of formation of species i at reactor inlet (kmol/m^3 cat/s)
S_K	selectivity of ketones
TON	turnover number (mol acid/mol basic active site/s)
X_A	fractional conversion of acid
(4-HN)	4-Heptanone
(3-HX)	3-Hexanone
(3-PN)	3-Pentanone

Greek symbols

ϵ	expansivity, change in number of moles (=0.165 for feed conditions used)
λ	wavelength of incident radiation
$\eta\varphi^2$	Weisz–Prater module
θ	peak position in degrees
τ	residence time (bed volume/volumetric flow rates)
ρ_{cat}	bulk density of catalyst (kg/m^3)

thermal methods and report improved stability and enhanced activity for acid-catalyzed and oxidation reactions. Drawbacks of the hydrothermal process include crystallization taking place in a closed vessel where side reactions can occur [29] and the challenge of controlling the extent of Ce incorporation because some Ce inevitably exist in the synthesis solution [30].

In this paper, we apply the citrate method described above to generate novel, catalytically active MnO_x/CeO_2 catalysts on HMS or MCM-41 mesoporous silica supports. The MnO_x is included at 10 mol% loading in CeO_2 because MnO_x at this level has been reported to enhance the activity of CeO_2 for the ketonization of propionic acid [21]. The catalysts prepared, abbreviated as CM-HMS and CM-MCM-41, are characterized by various analytical methods to understand their surface and structural properties. We also examine the catalytic activities of CM-HMS and CM-MCM-41 and compare them with unsupported MnO_x/CeO_2 for the ketonization of propionic acid (PA) and butyric acid (BA) and their mixtures.

2. Experimental

2.1. Materials and catalysts

2.1.1. Materials

All chemicals were purchased from Sigma–Aldrich and used without further purification. Nitrogen (99.99%), helium (99.999%), and carbon dioxide (99.998%) were obtained from Airgas.

2.1.2. Preparation of unsupported MnO_x(10 mol%)/CeO_2

Cerium nitrate hexahydrate ($Ce(NO_3)_3{\cdot}6H_2O$, 7.30 g, 0.017 mol) and 0.43 g (0.0017 mol) of manganese nitrate tetrahydrate ($Mn(NO_3)_2{\cdot}4H_2O$) were dissolved in deionized water and then hydrolyzed with aqueous ammonia at room temperature. After washing with water, the hydrolyzed material was dried at 80 °C for 24 h and then calcined at 170 °C and 550 °C for 2 h and 3 h in air, respectively, to obtain a 10 mol% MnO_x in CeO_2 catalyst, hereafter referred to as MnO_x/CeO_2.

2.1.3. Hexagonal mesoporous silica (HMS)

Wormhole hexagonal mesoporous silica (HMS) was prepared by a neutral S^0I^0 templating route using the following procedure: Dodecylamine (5.00 g, 0.027 mol) was dissolved in ethanol (41.47 g, 0.9 mol) and distilled water (28.80 g, 1.6 mol). After a clear solution was formed, tetraethyl orthosilicate (TEOS, 20.83 g, 0.1 mol) was added under vigorous stirring. The material was aged for 18 h at room temperature, after which the liquid was decanted and the solid was dried on a glass plate at room temperature. Finally, the template was removed by calcination at 650 °C for 3 h in air to obtain the HMS.

2.1.4. MCM-41

MCM-41 was purchased from Sigma–Aldrich and used without modification.

2.1.5. Preparation of CM-HMS and CM-MCM-41

Cerium nitrate hexahydrate ($Ce(NO_3)_3{\cdot}6H_2O$, 7.30 g, 0.017 mol), manganese nitrate tetrahydrate ($Mn(NO_3)_2{\cdot}4H_2O$, 0.43 g, 0.0017 mol), and citric acid monohydrate (7.85 g, 0.0374 mol) were individually dissolved in deionized water, and the solutions were then mixed. The molar ratio of total metals (Ce+Mn) to citric acid is 1:2. The aqueous solution containing nitrates of cerium and manganese and citric acid was added to 3.62 g of HMS or MCM-41 by the incipient wetness technique. After addition, the material was dried in an oven at 80 °C for 24 h under vacuum to obtain a metal–citrate complex in HMS and MCM-41. It was then calcined at 170 °C and 550 °C for 2 h and 3 h in air, respectively, in order to obtain the active mesoporous base catalysts denoted as CM-HMS and CM-MCM-41. The CM-HMS and CM-MCM-41 materials contain 46 wt% MnO_x/CeO_2 (Scheme 1).

2.2. Catalyst characterization

2.2.1. Infrared spectroscopy

Infrared spectra of the samples pressed in KBr pellets were obtained at a resolution of 2 cm^{-1} between 4000 and 400 cm^{-1}. The spectra were collected with a Perkin Elmer Spectrum 2000 instrument, with each sample spectrum referenced against that of a blank KBr pellet.

2.2.2. Powder X-ray diffraction (XRD)

XRD patterns were obtained using Cu Kα radiation (λ = 1.540562 Å). Samples were step-scanned from $2\theta = 1$–$70°$ in 0.045° steps with a stepping time of 0.5 s. Average particle sizes were calculated from the line broadening of the XRD peaks using the Scherrer equation:

$$d = \frac{k \cdot \lambda}{\mathrm{FWHM} \times \cos(\theta)} \tag{1}$$

In Eq. (2), k is 0.90, λ is the wavelength of the incident radiation, FWHM is the full width of the diffraction peak (degrees) at half maximum, and θ is the peak position in degrees.

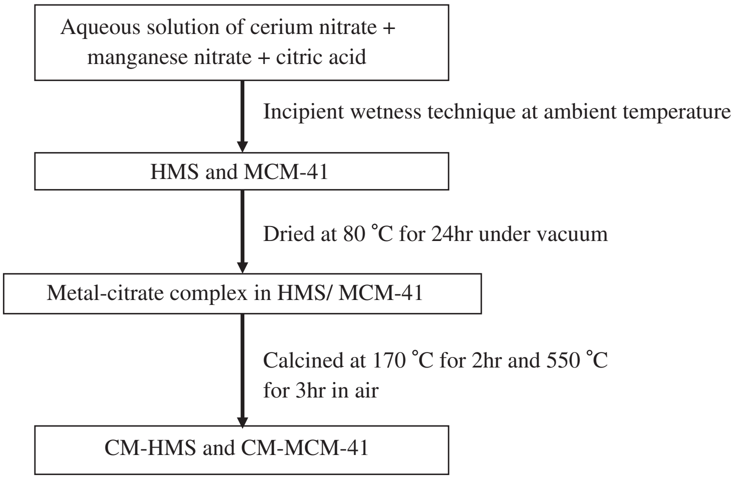

Scheme 1. Schematic representation of CM-HMS and CM-MCM-41 catalyst preparation.

2.2.3. N_2 adsorption measurements

Surface area measurements and pore size distribution analysis were done by nitrogen adsorption at 78 K in a Micromeritics ASAP 2010 instrument. Prior to measurements, the sample was outgassed in the degas port of the apparatus at 120 °C for 24 h.

2.2.4. Transmission electron microscopy (TEM)

TEM studies were performed on a JEOL (2200FS) electron microscope equipped with a field emission gun. All images were taken at 200 kV using with a 1024 × 1024 Gatan multiscan camera. Catalyst samples were first suspended in ethanol and then placed as a droplet onto a wholly carbon-coated copper grid, followed by air drying before analysis.

2.2.5. Energy-dispersive X-ray spectrometry (EDX)

EDX studies were performed by analyzing the samples using an Oxford EDX spectrometer equipped with Oxford INCA acquisition and analysis software.

2.2.6. Diffuse reflectance UV–visible (UV–vis)

UV-Vis diffuse reflectance spectra were recorded over the wavelength range $\lambda = 200–600$ nm using a Perkin Elmer (Lambda 900) UV–vis-NIR spectrophotometer.

2.2.7. Temperature-programmed desorption (TPD) of CO_2

CO_2-TPD measurements were performed by volumetric adsorption in a Micromeritics AutoChem 2910 instrument. A thermal conductivity detector and an Ametek Dycor M100M Quadrupole Mass Spectrometer were used for continuous monitoring of the desorbed CO_2. Prior to CO_2 adsorption, approximately 0.330 g of catalyst was thermally pretreated in He (99.999%) at a flow rate of 50 $cm^3\ min^{-1}$ either at 410 °C for 1 h or at 700 °C for 3 h, followed by cooling to room temperature in He. After pretreatment, each catalyst was saturated at room temperature with CO_2 (99.998%) at a flow rate of 50 $cm^3\ min^{-1}$ for 1 h and then subsequently purged with He (50 $cm^3\ min^{-1}$) for 2 h to remove all physisorbed CO_2. The desorption of chemisorbed CO_2 was carried out in He flow with the catalyst being heated from ambient temperature to 700 °C at a rate of 10 °C min^{-1} and held for 30 min. The resulting CO_2 peak was quantified by calibrating the area using a CO_2 gas standard.

2.3. Reaction procedure and analysis

Ketonization of carboxylic acids was carried out at 410 °C and atmospheric pressure under N_2 at a flow rate of 15 $cm^3\ min^{-1}$ in a fix-bed catalytic reactor equipped with a downstream condenser. In a typical run, 1.5 g of catalyst was loaded into the reactor between quartz beads (above) and quartz wool (below) and preheated in N_2 to 410 °C for 1 h prior to the reaction. The reactor was maintained under isothermal conditions during all runs. Liquid propionic acid (PA), butyric acid (BA), or a mixture of the two was fed into the reactor at the flow rate of 6 $cm^3\ h^{-1}$ by an HPLC pump. The reactor effluent was collected in a tube connected to the downstream condenser and immersed in a dry ice and acetone bath.

For ketonization of propionic acid (PA), the effluent was analyzed using a high-pressure liquid chromatograph that includes a Waters 717 autosampler, Waters 410 differential refractometer, and a Perkin-Elmer LC90 UV detector. The analysis was done on an Aminex HPX87H column using H_2SO_4 (5 mM) in water (0.6 ml min^{-1}) as a mobile phase. For butyric acid (BA) and mixtures of PA with BA, the liquid effluent was analyzed using a Hewlitt–Packard Model 5890 gas chromatograph equipped with a thermal conductivity detector (TCD). An EC-WAX capillary column (15 m, 0.53 mm ID, film thickness 1.20 μm), heated with a temperature profile from 40 to 250 °C at 20 °C min^{-1}, was used with helium as carrier gas at a flow rate of 15 ml min^{-1}. The gaseous products for all reactions were analyzed by gas chromatography (Varian 3300) with TCD using a packed column (Porapack Q) heated from 40 to 220 °C at 30 °C min^{-1}, with helium as carrier gas.

The catalytic activities of CM-HMS, CM-MCM-41, and unsupported MnO_x/CeO_2 catalysts for PA or BA ketonization were compared in terms of turnover number (TON) by treating the ketonization reaction as an irreversible second-order reaction.

$$-r_i = kC_i^2 \tag{2}$$

where species "*i*" represents either PA or BA. Accounting for the change in number of moles in reaction, the rate expression can be integrated to find the rate constant *k* (m^6/kmol/kg cat/s) at reaction conditions.

$$2 \in (1+\in)\ln(1-X_A) + \in^2 X_A + (\in+1)^2 \frac{X_A}{(1-X_A)} = kC_0\tau \times \rho_{cat} \tag{3}$$

In Eq. (3), C_0 is an initial concentration of acid at reaction conditions (kmol/m^3), X_A is fractional conversion of acid, τ is residence time (reactor bed volume/volumetric flow rates), ρ_{cat} is a bulk density of catalyst (kg/m^3), and ε is expansivity (=0.165 at feed conditions) related to net change in number of moles during reaction.

The TON (mol acid/mol basic active site/s) at the reactor inlet is then calculated using the following expression.

$$\mathrm{TON} = \left(\frac{kC_0^2}{C_T}\right) \tag{4}$$

where k is the rate constant, C_0 is the feed concentration of acid (kmol/m^3), and C_T is the basic site concentration in the catalyst (kmol/kg cat).

In the reaction of PA and BA, selectivity to ketones, S_K, is expressed as

$$S_k = \frac{2 \times N_k}{(N_a - N'_a)} \tag{5}$$

where N_a, N'_a, and N_k are molar flow rates of acid feed, exiting unreacted acid, and ketone produced in the reactor, respectively. The ketone yield for mixed PA and BA feeds is given as

$$\mathrm{Yield}_{(k)}\ (\%) = \frac{2 \times N_k}{N_a} \times 100 \tag{6}$$

where N_a is the total molar feed rate of acids and N_k is the molar rate of the produced ketones.

3. Results and discussion

3.1. Catalyst characterization

3.1.1. FTIR

Since CM-HMS and CM-MCM-41 catalysts were prepared by the citrate process, it is helpful to evaluate the interaction between metal and citric acid in HMS and MCM-41. The FTIR spectra of citric acid and metal–citrate complexes that are formed in HMS and MCM-41 in the region 2000–1000 cm^{-1} are shown in Fig. 1. Literature data [31] provide reliable identification of the principle adsorption bands for citric acid (Fig. 1a). In the C═O stretching region, two carbonyl peaks are obtained: the peak at 1757 cm^{-1} is indicative of free carboxylic acid groups, whereas the peak at 1690 cm^{-1} represents coordinated carboxyl groups, i.e. groups showing internal hydrogen bonds. The bands in the ranges 1350–1430 and 1166–1258 cm^{-1} correspond, respectively, to the C—O stretching vibrations and to —OH in-plane deformation vibrations. The —OH stretching vibrations of the carboxylic acid groups occur as a broad band with two superimposed peaks (—OH bonding at ~3500 cm^{-1} and intermolecular H-bond at ~3305 cm^{-1}, not shown). Finally, C—O stretching in the C—OH group and tertiary —OH are represented by the bands at 1080 and 1125 cm^{-1}, respectively. In the metal–citrate complex formed in HMS and MCM-41 (Fig. 1b and Fig. 1c), carboxylate salts are present. The resonance between the two C—O bonds of the COO$^-$ groups results in the appearance of bands near 1614 cm^{-1} and 1434 cm^{-1} that correspond to the asymmetric and symmetric vibrations [32]. Many other skeletal vibrations occur in the range of 1437–1300 cm^{-1}, so the band at 1614 cm^{-1} best characterizes the carboxylate group attached to metallic ions [31]. Thus, the absence of free carboxylic acid groups (1690–1757 cm^{-1} (Fig. 1b and c)) indicates that citric acid is forming a complex either with Ce or with Mn ions in HMS and MCM-41, which is an essential precursor for the formation of a uniform solid solution of mixed metal oxides. Other bands from the metal–citrate complex in HMS and MCM-41 (Fig. 1b and c) can be attributed to the C—O stretching of the C—OH group (1088 cm^{-1}) and to —OH bending (1236 cm^{-1}), respectively, while the sharp absorption band of the nitrate ions can be seen at 1385 cm^{-1}.

The FTIR absorption spectra of HMS, MCM-41, and calcined CM-HMS and CM-MCM-41 samples are shown in Fig. 2. All samples show characteristic absorption bands at 3496 cm^{-1} (not shown) and 1687 cm^{-1} assigned to overlapping of the —OH stretching of adsorbed water and silanols. In the range of 400–1600 cm^{-1}, peaks at 480 cm^{-1}, 844 cm^{-1}, 1125 cm^{-1}, and 1234 cm^{-1} correspond to the rocking, bending (or symmetric stretching), and asymmetric stretching of the inter-tetrahedral oxygen atoms in SiO$_2$, respectively. In Fig. 2b and d, a small absorption band at ~963 cm^{-1} in CM-HMS and CM-MCM-41 is seen, suggesting formation of Si—O—M$^+$ (Ce and Mn) linkages and thus a small degree of incorporation of MnO$_x$/CeO$_2$ into the silica framework of HMS and MCM-41. The results are in accordance with earlier literature reports [23,27]. The absence of carbonyl bands in the calcined CM-HMS and CM-MCM-41 suggests that all organic functionalities were decomposed during calcination. The FTIR spectra indicate that during the preparation of CM-HMS and CM-MCM-41, the metal–citrate complex in HMS and MCM-41 is formed. This complex is decomposed during the calcination step, and MnO$_x$/CeO$_2$ is partially incorporated into the framework of HMS and MCM-41.

3.1.2. Powder X-ray diffraction

Low-angle XRD patterns of HMS, MCM-41, CM-HMS, and CM-MCM-41 are shown in Figs. 3 and 4. The d_{100} values calculated using the equation

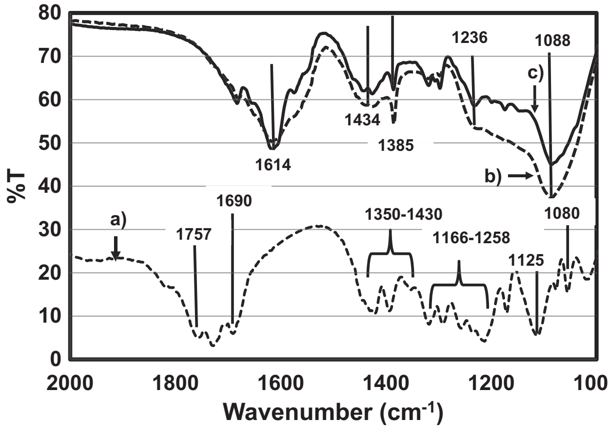

Fig. 1. FTIR spectra of (a) citric acid; (b) metal–citrate complex in HMS; (c) metal–citrate complex in MCM-41.

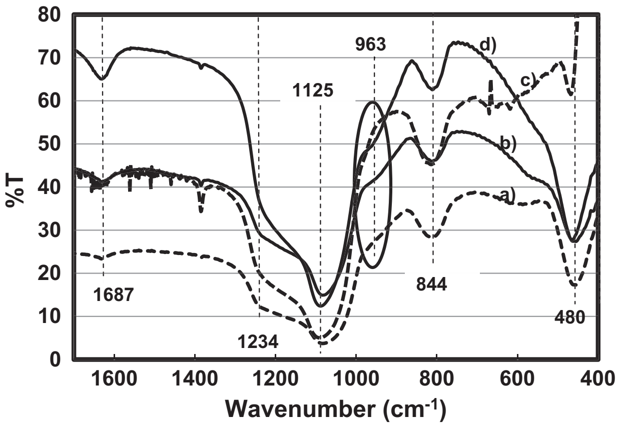

Fig. 2. FTIR Spectra of (a) - - - - - MCM-41; (b) — CM-MCM-41; (c) – HMS; (d) — CM-HMS.

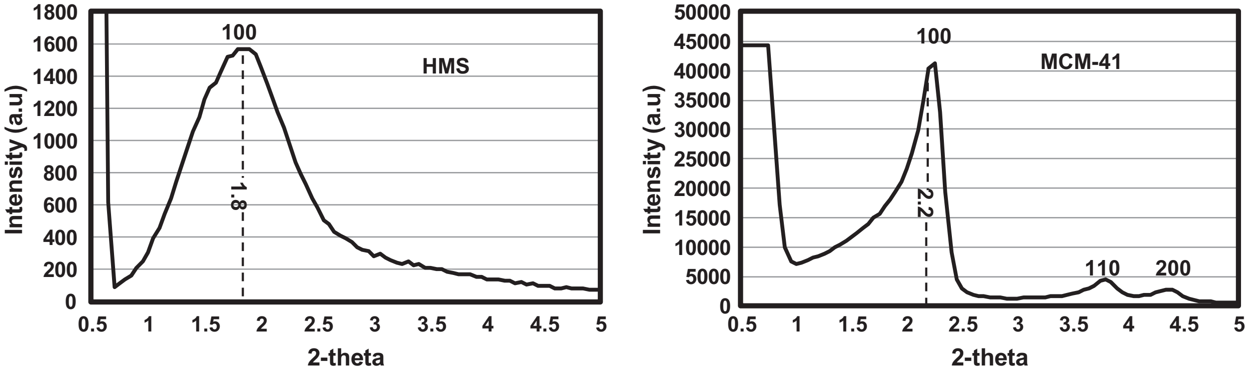

Fig. 3. Low-angle XRD of HMS and MCM-41.

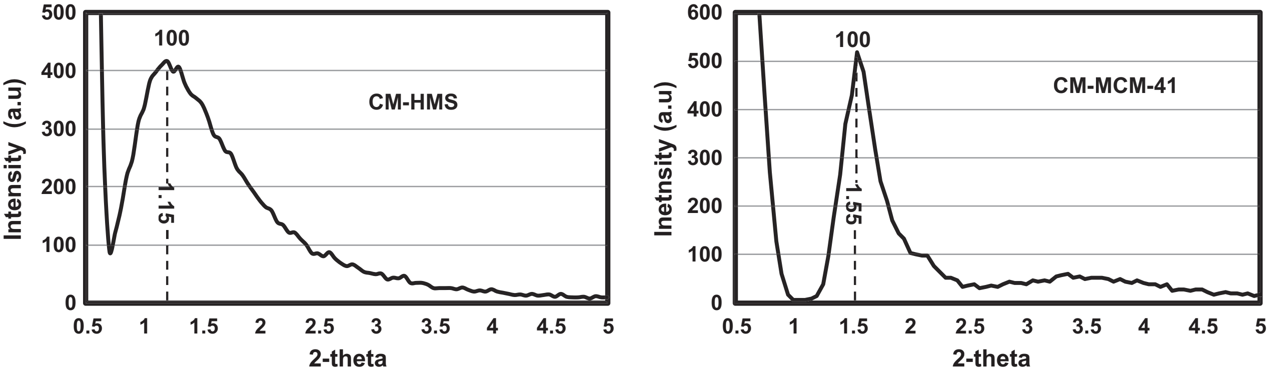

Fig. 4. Low-angle XRD of CM-HMS and CM-MCM-41.

Table 1
Unit cell (a_0) and d_{100} spacing parameters from XRD analysis.

Catalyst	d_{100} (nm)	a_0 (nm)
HMS	4.90	5.65
MCM-41	3.92	4.53
CM-HMS	7.66	8.84
CM-MCM-41	5.70	6.58

$$d_{100} = \frac{n\lambda}{2\sin\theta} \tag{7}$$

and the corresponding unit cell parameters (a_0) of HMS, MCM-41, CM-HMS, and CM-MCM-41 calculated from the peak $(h\,k\,l) = (1\,0\,0)$ using the following equation and are given in Table 1.

$$a_0 = 2\sqrt{3}d_{100} \tag{8}$$

In Fig. 3, HMS displays a strong, broad diffraction peak at $2\theta = 1.8°$, corresponding to the diffraction plane (1 0 0) of the typical hexagonal mesoporous silica wormhole structure assembled from long alkyl chain neutral amines as surfactants. This single, low-angle peak arises because of short-range hexagonal symmetry with uniform pore diameter [33]. Diffraction peaks of higher order are not observed, indicating that these materials do not possess significant long-range order. The absence of a long-range order can be attributed to the weak bonding forces (between the amine and silicates species) that govern the neutral (S^0I^0) pathway assembly [33]. On the other hand, MCM-41 shows three peaks at $2\theta = 2.2°$, 3.75°, and 4.35°, which correspond to a prominent peak for $(h\,k\,l) = (1\,0\,0)$ as well as weaker peaks for $(h\,k\,l) = (1\,1\,0)$ and (2 0 0) (Fig. 3). These peaks suggest that the MCM-41 material examined has hexagonal lattice symmetry as expected.

The CM-HMS and CM-MCM-41 catalysts show broad (1 0 0) diffraction peaks at $2\theta = 1.15°$ and $2\theta = 1.55°$, respectively, (Fig. 4), indicating deorganization of the mesoporous structure upon addition of MnO_x/CeO_2. Although the collapse of mesoporous channels could be responsible for the peak shift, we believe that the incorporation of MnO_x/CeO_2 into the mesopores of HMS and MCM-41 is the cause of such irregularity. This idea is supported by the shift in (1 0 0) peak locations to lower angle, reduction in peak intensity, and broadening of the (1 0 0) peak in both CM-HMS and CM-MCM-41 relative to the supports alone. The decrease in diffraction peak intensity of CM-HMS and CM-MCM-41 may be attributed to the decrease in diffraction contrast between the pores and the walls as a result of mesopores being partially filled with cerium and manganese oxides. The *d*-spacing (d_{100}) and unit cell parameter (a_0) of both supports and CM-HMS and CM-MCM-41 are given in Table 1. While it is possible that the increase in d_{100} and a_0 for CM-HMS and MC-MCM-41 results from incorporation of Ce and Mn into the mesoporous silica structure (as has been reported [23,27] for Ce-containing MCM-41 prepared by hydrothermal methods), we consider this unlikely given that Ce and Mn are deposited into the silica framework after the silica structure has been established and show only slight incorporation into the silica framework according to our FTIR data. It is more likely that MnO_x/CeO_2 is deposited onto the mesopore walls of the silica framework, increasing the framework wall thickness (FWT, see below) and unit cell parameter.

The wide-angle XRD spectra of HMS and MCM-41 show only a broad peak of amorphous silica at $2\theta = 22°$ (Fig. 5). The XRD peaks for CM-HMS and CM-MCM-41 are observed at $2\theta = 28.1°$, 33.1°,

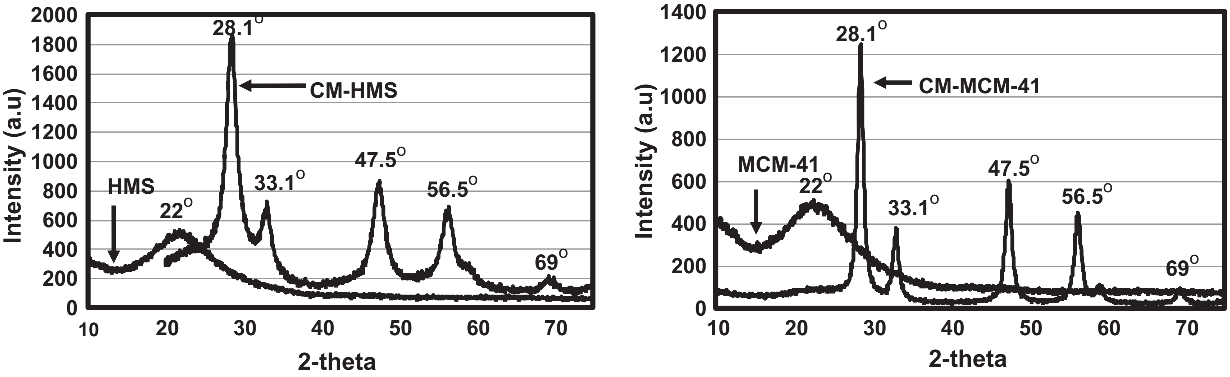

Fig. 5. Wide-angle XRD of HMS, MCM-41, CM-HMS, and CM-MCM-41.

47.5°, and 56.5°, corresponding to (1 1 1), (2 0 0), (2 2 0), and (3 1 1) planes, respectively. These diffraction peaks are characteristic of the cubic ceria phase with a fluorite structure. No peaks characteristic of MnO$_x$ are seen in CM-HMS and CM-MCM-41, evidence that MnO$_x$ is fully dispersed as a solid solution in CeO$_2$. The presence of diffraction peaks of CeO$_2$ in the XRD spectrum of CM-HMS and CM-MCM-41 indicate that some particles of CeO$_2$ are dispersed on the surface of HMS and MCM-41, as particles present within the support pores would be too small to create a diffraction pattern. From the wide-angle XRD data, the average particle sizes of CeO$_2$ present on surface of HMS and MCM-41, calculated using Eq. (2), are 6 nm and 15 nm, respectively.

Table 2
Surface area and pore properties of catalysts and supports from N$_2$ adsorption at 78 K.

Catalyst	BET surface area (m^2 g^{-1})	BJH average pore diameter (nm)	Pore volume (cm^3 g^{-1})	FWT[a] (nm)
HMS	782	5.4	1.10	0.25
MCM-41	1184	3.7	1.23	0.83
CM-HMS	250	4.2	0.30	4.60
CM-MCM-41	529	3.4	0.54	3.10
MnO$_x$/CeO$_2$	106	10.3	0.29	ND

[a] Framework thickness (FWT) = unit cell (a_0) − pore diameter. ND = not determined.

3.1.3. N$_2$ adsorption measurements

The nitrogen adsorption isotherms of HMS, MCM-41, CM-HMS, and CM-MCM-41 are shown in Fig. 6. The isotherms of all samples are Type IV according to the IUPAC classification [34], with a sharp step at intermediate relative pressures. The hysteresis loop for these samples starts at a relative pressure of p/p_0 = 0.3–0.45, indicating the presence of mesoporosity. This hysteresis loop extends to a relative pressure of $p/p_0 \geqslant 0.80$, implying that there is a textural inter-particle mesoporosity or macroporosity. The sharp inflection of the adsorption branch confirms the uniform mesoporosity of the supports, and the appreciable type H1 hysteresis loops in all samples indicate the presence of textural and cylindrical mesopores.

The BET surface area (S_{BET}), average pore volume (V_{p}), average pore diameter calculated by the Barrett–Joyner–Halenda (BJH) method, and framework thickness (FWT) calculated by subtracting the unit cell parameter (a_0) from the pore diameter of HMS, MCM-41, CM-HMS, and CM-MCM-41 are listed in Table 2. Given that the MnO$_x$/CeO$_2$ loading on HMS and MCM-41 supports is 46% by weight, the decrease in BET surface area and in pore volume of nearly 50%, along with the commensurate increase in framework thickness (FWT), indicates that MnO$_x$/CeO$_2$ is deposited onto the walls of the HMS and MCM-41 mesopore supports. Following the rationale set forth by Zukal et al. [35] in calculating normalized pore volume (NPV) and normalized pore diameter (NPD), it appears that wall deposition and not pore blocking is responsible for the decrease in pore diameter. Along this line, the calculation of Xu et al. [36] suggests that approximately 85% of the MnO$_x$/CeO$_2$ is estimated to be deposited along the mesopore walls of HMS, while about 35% is deposited along the mesopore walls of MCM-41. The remainder of the material should be present on support particle surfaces, as confirmed by the wide-angle XRD diffraction patterns.

3.1.4. TEM

The high-resolution TEM images of HMS and MCM-41 are displayed in Fig. 7. As-synthesized HMS shows a wormhole-like mes-

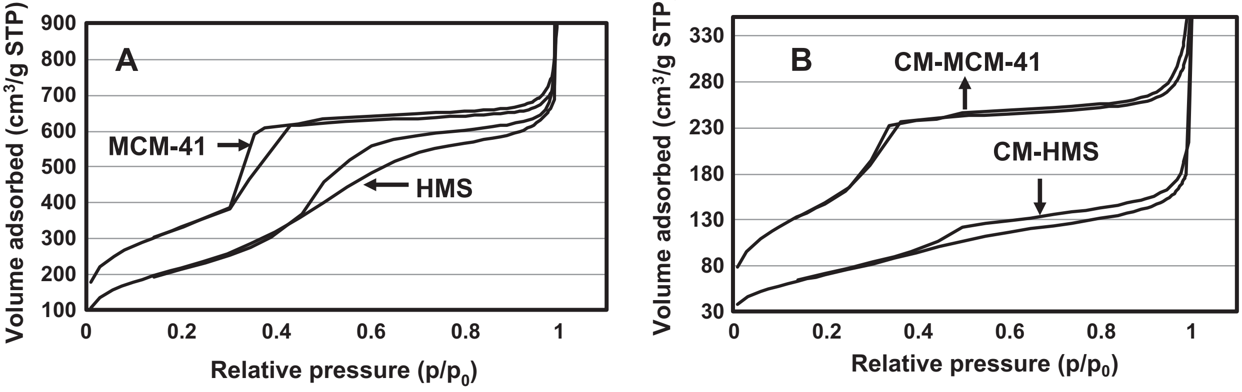

Fig. 6. N$_2$ adsorption isotherms: (A) HMS and MCM-41; (B) CM-HMS and CM-MCM-41.

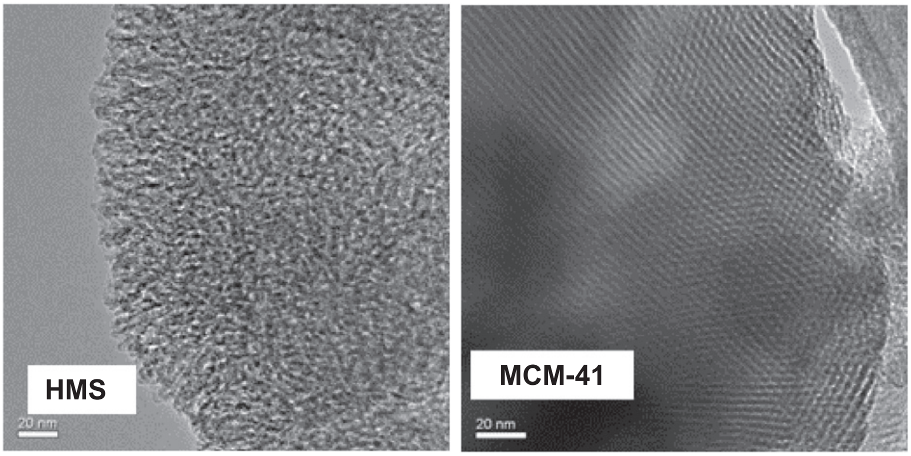

Fig. 7. TEM images of HMS and MCM-41.

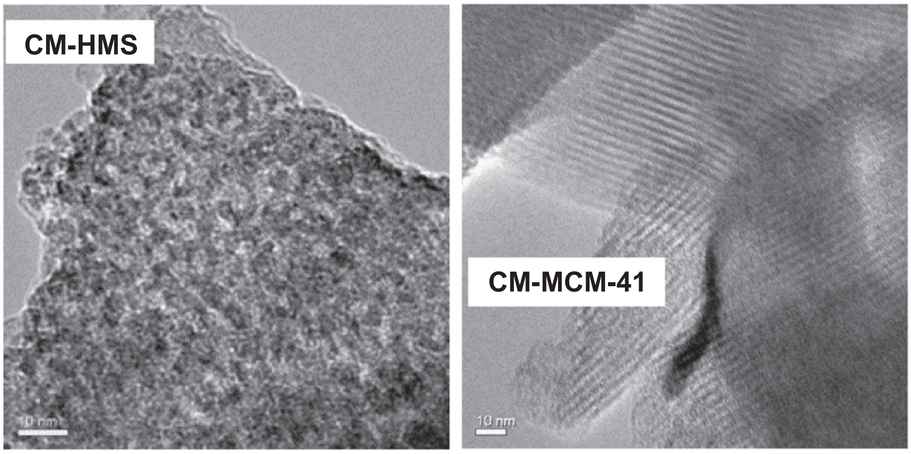

Fig. 8. TEM images of CM-HMS and CM-MCM-41.

oporous framework, and although long-range packing order is absent, a regular, uniform network of channels is observed [33]. In contrast, the TEM micrograph of MCM-41 shows a hexagonal structure with long-range ordered mesoporosity. TEM images of CM-HMS and CM-MCM-41 are shown in Fig. 8; the CM-HMS sample exhibits a wormhole structure, while CM-MCM-41 has well-ordered hexagonal arrays and one-dimensional long-range structure. Thus, the CM-HMS and CM-MCM-41 catalysts retain the mesoporous framework of HMS and MCM-41.

3.1.5. Energy-dispersive X-ray analysis (EDX)

The EDX spectra of CM-MCM-41 and CM-HMS are shown in Fig. 9, clearly confirming the presence of Ce and Mn in CM-HMS and CM-MCM-41. In order to obtain evidence of the uniform dispersion of oxides of cerium and manganese in CM- HMS and CM-MCM-41, quantification of elemental composition using EDX was carried out at three arbitrary spots on different catalyst particles. The quantitative analysis of Ce, Mn, and Si at three different arbitrary spots showed no significant change in relative intensities. This provides strong indication that most of the Ce and Mn are uniformly distributed into or onto the support materials.

3.1.6. Diffuse reflectance UV–visible (UV–vis)

Diffuse reflectance UV–visible spectroscopy has been used extensively to study ceria-based materials and transition metal oxides to obtain information on surface coordination and different oxidation states of metal ions by measuring their d–d and f–d transitions and oxygen–metal ion charge transfer bands [37]. Diffuse reflectance (DR) UV–vis spectroscopy is known as a very sensitive probe for the characterization of metal ion coordination of metal-containing mesoporous materials. The position of ligand to metal charge transfer ($O^{2-} \rightarrow Ce^{4+}$) spectra depends on the ligand field symmetry surrounding the Ce center. Therefore, this technique gives valuable information about existence of metal ions in the framework and/or exterior to the framework position [23]. The CM-HMS and CM-MCM-41 catalysts show a single broad peak in the DR UV–vis spectra centered at 294 nm (Fig. 10). This peak can be attributed to the electronic transition with charge transfer ($O^{2-} \rightarrow Ce^{4+}$) associated with Ce ions in SiO_2 of HMS and MCM-41. The electronic transitions from oxygen to cerium require higher energy for a tetra-coordinated Ce^{4+} than for the hexa-coordinated metal atom. Therefore, it can be inferred that the single absorption band centered at 294 nm for CM-MCM-41 and CM-HMS catalyst is due to the presence of one type of highly dispersed Ce^{4+} species in a tetra-coordinated environment in the silica network of CM-HMS and CM-MCM-41. As expected, the electronic spectra of HMS and MCM-41 did not show any electronic transition.

It is clear from the FTIR, low-angle powdered XRD, pore diameter, pore volume, framework thickness, UV-vis, and TEM data that the most of the particles of MnO_x/CeO_2 in CM-HMS and CM-MCM-

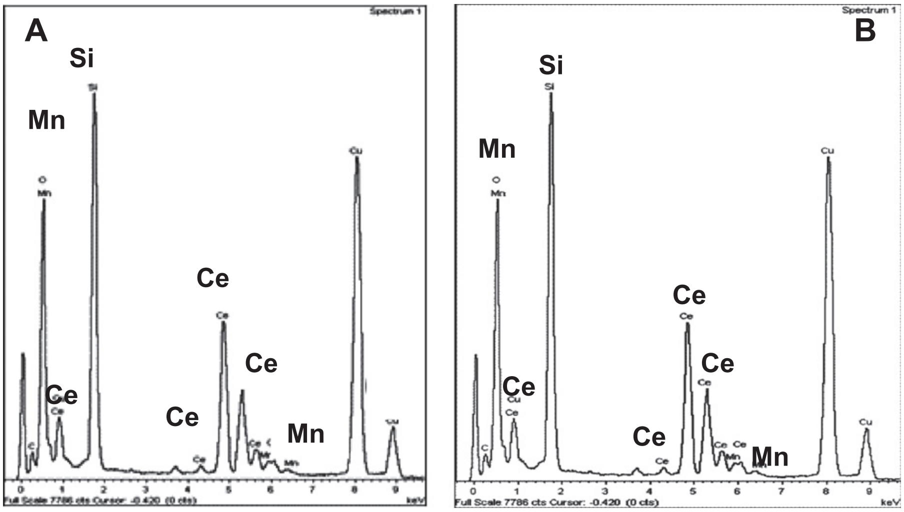

Fig. 9. EDX of (A) CM-HMS; (B) CM-MCM-41.

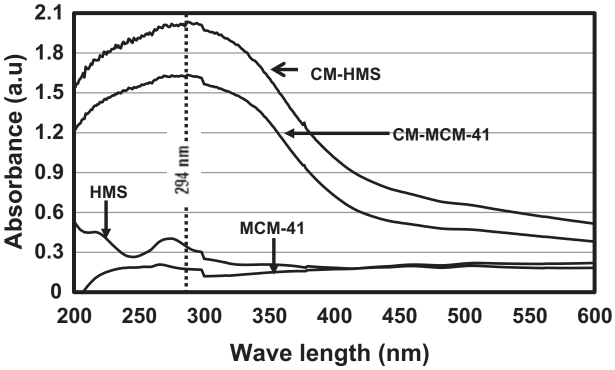

Fig. 10. Diffuse reflectance UV–visible of HMS, MCM-41, CM-HMS, and CM-MCM-41.

41 are located in the framework or walls of silica matrix of HMS and MCM-41, respectively, and other particles are highly dispersed on the surface of HMS and MCM-41 as confirmed by wide-angle XRD and BET surface area results.

3.1.7. CO_2-TPD

To understand the basic properties of unsupported MnO_x/CeO_2, CM-HMS, and CM-MCM-41, a temperature-programmed CO_2 desorption study was undertaken. In general, CO_2-TPD measurements provide meaningful information about the number of basic catalyst sites (since one CO_2 molecule adsorbs onto one basic site) [38], and about basic site strength as characterized by the temperature of the CO_2 desorption peak maximum (T_{max}).

Prior to CO_2 adsorption, two different thermal pretreatment conditions were used to remove surface-adsorbed species from each catalyst: the first was at 410 °C in He for 1 h, and the second was at 700 °C in He for 3 h. The pretreatment at 410 °C did not affect catalyst structure, because all catalysts were calcined at 550 °C in air for 3 h during preparation. However, as shown in Table 3, the catalyst pretreatment at 700 °C for 3 h in He significantly reduced BET surface area of the catalysts. Because reaction takes place at 410 °C, the pretreatment at 700 °C produced a significantly different catalyst structure and thus different active site density than what is present in reaction. Therefore, CO_2-TPD measurements on the 410 °C pretreated catalysts were used as the more appropriate characterization of the catalysts in the reaction environment.

Table 3
Effect of pretreatment temperature on surface area.

Catalyst	Pretreatment temperature (°C)	BET surface area (before pretreatment) ($m^2\,g^{-1}$)	BET surface area (after pretreatment) ($m^2\,g^{-1}$)
MnO_x/CeO_2	700	106	14
CM-HMS	700	250	168
CM-MCM-41	700	529	388

During all CO_2-TPD experiments, effluent gas was continuously monitored by mass spectrometry and via thermal conductivity detection in the 2910 instrument. As shown in Fig. 11, unsupported (bulk) MnO_x/CeO_2 exhibits three CO_2 desorption peaks, the first at 72 °C, a second at a slightly higher temperature of 120 °C, and a third, broad peak at 502 °C. In contrast, the CO_2-TPD profiles of supported CM-HMS and CM-MCM-41 catalysts (Figs. 12 and 13) show CO_2 peaks only at 63 °C for CM-HMS and at 69 °C for CM-MCM-41, with the rest of the peaks attributed to H_2O desorption. It is not known why bulk MnO_x/CeO_2 exhibits the CO_2 desorption peak at 502 °C (indicative of strongly basic sites), but it is clear that CM-HMS and CM-MCM-41 possess only weakly basic sites. The basic site density for both bulk and supported MnO_x/CeO_2 is therefore based only on the low-temperature desorption peaks.

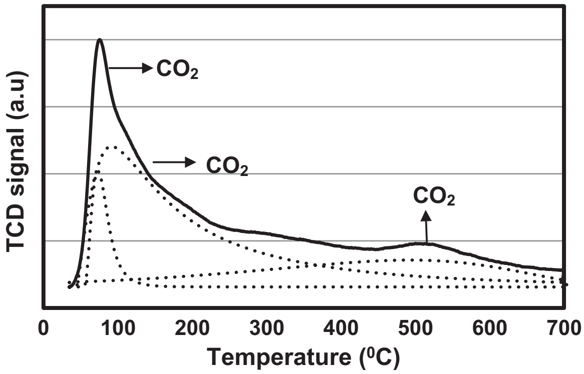

Fig. 11. TPD profile of bulk MnO_x/CeO_2.

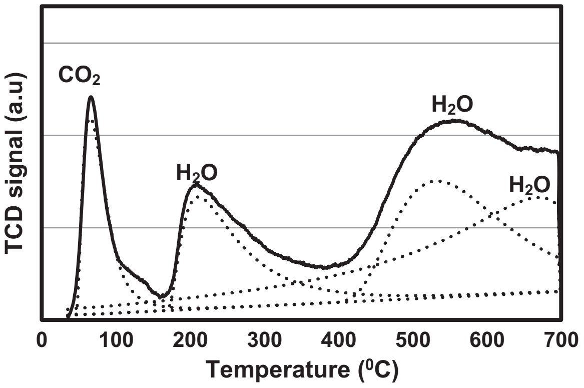

Fig. 12. TPD profile of CM-HMS.

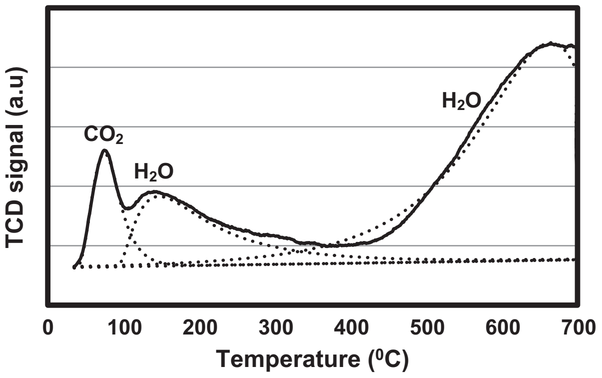

Fig. 13. TPD profile of CM-MCM-41.

In view of the generation of water from CM-HMS and CM-MCM-41, a control experiment of CO_2-TPD analysis on pure HMS and MCM-41 was performed (not shown). As expected, no CO_2 desorption was observed from HMS and MCM-41, but the same peaks associated with water seen in Figs. 12 and 13 were observed, suggesting that water is present in or generated from the silica supports even after pretreatment at 410 °C.

3.2. Catalytic reactions

3.2.1. Ketonization of propionic acid (PA) and butyric acid (BA)

The catalytic activities of CM-HMS, CM-MCM-41, and unsupported MnO_x/CeO_2 for ketonization were characterized at 410 °C in the atmospheric pressure fixed-bed reactor. In all reactions, the selectivity to ketone formation was >98%, and no products other than water and carbon dioxide were observed. The material balance in all experiments closed to 100 ± 5%. The stabilities of CM-HMS and CM-MCM-41 were also studied for ketonization of PA over 20 h of continuous operation; no significant drop in conversion of PA or in selectivity toward 3-pentanone was observed.

Two different catalyst bed sizes were used for propionic acid ketonization; Fig. 14 shows a plot of Eq. (3) for both CM-HMS and CM-MCM-41. The straight line observed in Fig. 14 verifies that the PA ketonization reaction follows simple second-order kinetics. Assuming BA ketonization also follows second-order kinetics, the second-order rate constant (from the slope of plots in Fig. 14) and turnover number (TON) are reported in Table 4 for PA and in Table 5 for BA.

The absence of internal diffusion resistances in ketonization was verified by calculating the Weisz–Prater module ($\eta\varphi^2$) for the reaction

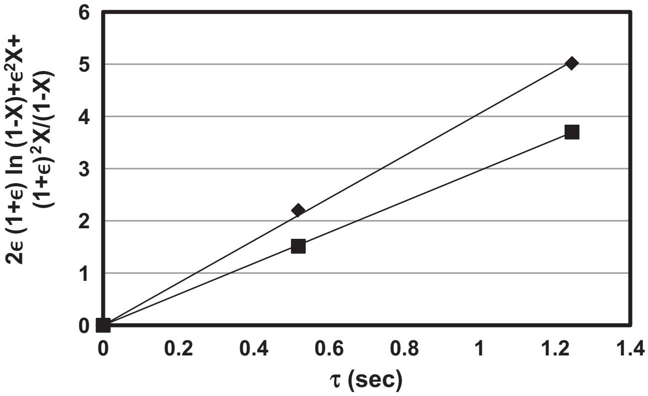

Fig. 14. Plot of Eq. (3) that demonstrates second-order behavior of ketonization reaction (◆) – CM-HMS; (■) – CM-MCM-41.

$$\eta\varphi^2 = \frac{(-r_{i,o})D_P^2}{D_{effC_o}} \tag{9}$$

where $-r_{i,o}$ is the reaction rate (kmol/m^3 cat/s) at the inlet of the catalyst bed, D_{eff} is the effective diffusivity of PA ($D_{eff} \sim 4.8 \times 10^{-6}$ m^2/s) as estimated by the Chapman–Enskog equation, C_0 is the initial concentration of acid feed ($C_0 = 0.012$ kmol/m^3), and D_p is the catalyst support particle diameter, ($D_p \sim 4 \times 10^{-6}$ m) obtained from SEM. For MnO_x/CeO_2 catalyst and PA ketonization, $\eta\varphi^2 \sim 1 \times 10^{-5}$, indicating that the reaction is kinetically controlled. Since the average particle size, conversions, and initial concentration of acids are similar for all catalysts, we conclude that reactions performed over CM-HMS and CM-MCM-41 are likewise kinetically controlled.

In order to understand the role of mesoporous silica support in the activity of CM-HMS and CM-MCM-41, a control experiment was performed in which PA was passed through the MCM-41 alone support under reaction conditions. As seen in Table 4, MCM-41 alone is inactive for the ketonization of PA.

Because the supported CM-HMS and CM-MCM-41 catalysts showed only the presence of weakly basic sites as evidenced by the CO_2 desorption peak at 63 and 69 °C, turnover numbers (TON, Eq. (3)) were based on the weakly basic site densities for both bulk and supported MnO_x/CeO_2 catalysts. As presented in Tables 4 and 5, the TON determined for CM-HMS and CM-MCM-41 is found to be similar to that for unsupported MnO_x/CeO_2. However, since the fractional conversion of feed acid was approximately the same for both bulk and supported catalysts, the MnO_x/CeO_2 catalyst is more efficiently utilized in the supported CM-HMS and CM-MCM-41 than in the bulk material because CM-HMS and CM-MCM-41 contain only 46 wt% MnO_x/CeO_2. Based on the CO_2-TPD results and agreement between bulk and supported TON, it can be inferred that weakly basic sites of MnO_x/CeO_2 are primarily responsible for the ketonization of carboxylic acids.

3.2.2. Ketonization of propionic acid (PA) and butyric acid (BA) mixtures

The catalytic activity of CM-MCM-41 was further evaluated in the ketonization of a mixture of PA and BA to form three ketone products 3-pentanone (3-PN), 3-hexanone (3-HX), and 4-heptanone (4-HN) as shown in Scheme 2. Equimolar quantities of each acid were fed to the reactor at a combined rate equal to that of single acids in other experiments, such that the individual inlet concentrations of PA and BA were one-half the values used in experiments where the acids were individually fed.

The rate constants for the three reactions shown in Scheme 2 were adjusted to correctly predict outlet concentrations of acids

Table 4
Catalyst activity for propionic acid (PA) ketonization.

Catalyst	Catalyst loading in reactor (g)	Conversion of PA (%)	Rate constant (*k*) (m^6/kmol/s/kg cat)	Basic site concentration (C_T) (kmol/kg × 10^5)	TON*
MCM-41	1.5	0	0	0	0
MnO_x/CeO_2	1.5	80	0.60	3.2	2.7
CM-HMS	1.5	78	0.54	2.6	3.0
	0.62	63			
CM-MCM-41	1.5	73	0.39	2.8	2.0
	0.62	55			

Reaction conditions: N_2 flow = 15 cm^3/min; PA feed rate = 0.1 ml/min; *T* = 410 °C.
* TON = (mol acid/mol basic sites/s).

Table 5
Catalyst activity for butyric acid (BA) ketonization.

Catalysts	Catalyst loading in reactor (g)	Conversion of BA (%)	Rate constant (k) (m^6/kmol/s/kg cat)	Basic site concentration (C_T) (kmol/kg × 10^5)	TON*
MnO_x/CeO_2	1.5	28	0.043	3.2	0.16
CM-HMS	1.5	36	0.063	2.6	0.30
CM-MCM-41	1.5	31	0.049	2.8	0.22

Reaction conditions: N_2 flow = 15 cm^3/min; BA feed rate = 0.1 ml/min; *T* = 410 °C.
* TON = (mol acid/mol basic sites/s).

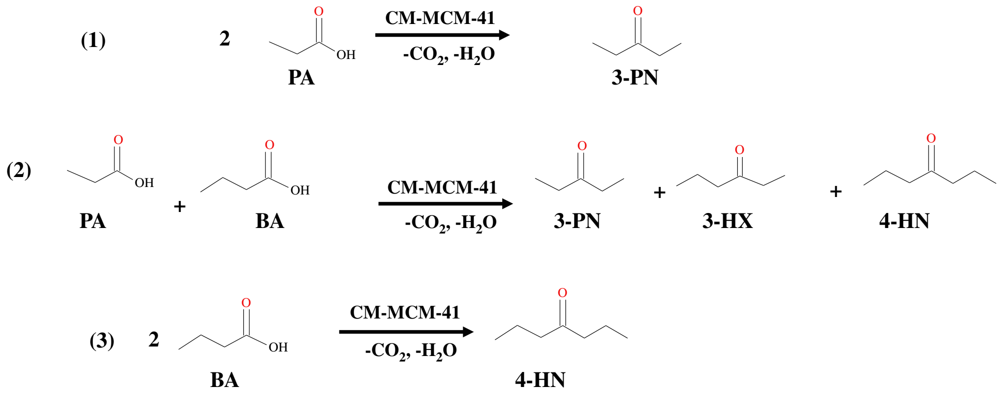

Scheme 2. Reaction scheme for ketonization of carboxylic acids.

and ketone products when the reactor balance equations were numerically integrated using Euler's method in Microsoft Excel. The composite rate constant for each acid is then determined as the sum of the two ketonization reactions in which the acid participates and is reported in Table 6. For PA, the value of 0.12 m^6/kmol/kg cat/s is approximately 1/3 the value of the rate constant for pure PA ketonization to 3-PN; for BA, the rate constant is 0.063 m^6/kmol/kg cat/s, 30% larger than the value for pure BA ketonization to 4-HN. The values of TON for PA and BA in this experiment were determined via Eq. (4) and are given in Table 6; values of TON are significantly lower because of the lower initial concentration of each acid in the mixture.

The increased rate of BA ketonization in the mixed acid ketonization is expected, as PA is significantly more reactive than BA and thus BA reacts more rapidly with PA than with BA. In fact, the rate constant for the cross-ketonization reaction (PA + BA) is approximately twice that of the (BA + BA) reaction, so the overall consumption rate of BA increases in the presence of PA.

In contrast, the presence of BA slows reaction of PA significantly. Because PA ketonization exhibits second-order behavior, it can be assumed that PA surface coverage on the catalyst during reaction is low enough such that rate is not inhibited by the adsorbed species (e.g. Langmuir–Hinshelwood behavior). We postulate that BA, although it is less reactive than PA, may adsorb somewhat more

Table 6
Activity of CM-MCM-41 for combined ketonization of propionic acid (PA) and butyric acid (BA).

Catalyst	Conversion (%)		Rate constant (*k*) (m^6/kmol/s/kg cat)		TON*		Yield of ketones (mol%)		
	PA	BA	PA	BA	PA	BA	3-PN	3-HX	4-HN
CM-MCM-41	38	14	0.12	0.063	0.14	0.074	10.50	14.02	3.35

Reaction conditions: Catalyst charge = 1.5 g; N_2 flow = 15 cm^3/min; Mole ratio PA:BA = 1:1; total acid feed rate = 0.1 ml/min; *T* = 410 °C.
* TON = (mol acid/mol basic sites/s).

strongly than PA on the catalyst, thus occupying sites and reducing the probability of adjacent PA–PA adsorption and reaction to 3-PN. Even relatively low surface coverage of BA could therefore significantly reduce PA ketonization rate, a concept that is supported by the formation of 3-HX in quantities greater than 3-PN.

4. Conclusions

The citrate method has been used to generate active centers of MnO_x/CeO_2 catalyst on two different types of mesoporous silica supports (HMS and MCM-41). FTIR spectroscopy results suggest that a metal–citrate complex is formed during the preparation of CM-HMS and CM-MCM-41. This complex is decomposed during the calcination step. FTIR results also show that MnO_x/CeO_2 is incorporated to a small degree into the silica matrix framework of HMS and MCM-41, but powder XRD, N_2 adsorption, and diffuse reflectance UV-vis studies reveal that most MnO_x/CeO_2 is present as particles on the walls of silica pore network of HMS and MCM-41, while the rest is highly dispersed on the surface of HMS and MCM-41. The EDX analysis confirms the particles of Mn and Ce are uniformly distributed over CM-HMS and CM-MCM-41 catalyst. The supported CM-HMS and CM-MCM-41 catalysts have better utilization of Ce and Mn than unsupported MnO_x/CeO_2 for ketonization of propionic acid and butyric acid, because they are distributed on the mesoporous support. A more uniform dispersion of MnO_x and CeO_2 apparently forms on HMS and MCM-41 than in the bulk catalyst, as evidenced by FTIR and UV-vis spectroscopy. Thus, CM-HMS and CM-MCM-41 hold significant promise as solid base catalysts to upgrade carboxylic acids to higher value intermediates or biofuel components.

Acknowledgment

Authors acknowledge financial support from the US Department of Energy Freedom Car Program, Grant DE-FC2607NT43278.

References

[1] C. Friedel, J. Liebigs, Ann. Chem. 108 (1858) 125.
[2] W.L. Howard, Encyclopedia of Chemical Technology (Kirk–Othmer), vol. 1, fourth ed., Wiley-Interscience, New York, 1998. p. 176.
[3] E.R. Squibb, J. Am. Chem. Soc. 17 (1895) 187.
[4] J.C. Kuriacose, R. Swaminathan, J. Catal. 14 (1969) 348.
[5] R. Swaminathan, J.C. Kuriacose, J. Catal. 16 (1970) 357.
[6] M. Jayamani, C.N. Pillai, J. Catal. 87 (1984) 93.
[7] R. Pestman, R.M. Koster, A. van Duijne, J.A.Z. Pieterse, V. Ponec, J. Catal. 168 (1997) 265.
[8] K.S. Kim, M.A. Barteau, J. Catal. 125 (1990) 353.
[9] R. Pestman, A. van Duijne, J.A.Z. Pieterse, V. Ponec, J. Mol. Catal. A 103 (1995) 175.
[10] R. Pestman, R.M. Koster, J.A.Z. Pieterse, V. Ponec, J. Catal. 168 (1997) 255.
[11] R. Martinez, M.C. Huff, M.A. Barteau, J. Catal. 222 (2004) 404.
[12] K. Okumura, Y. Iwasawa, J. Catal. 164 (1996) 440.
[13] K. Parida, H.K. Mishra, J. Mol. Catal. A 139 (1999) 73.
[14] M. Gliňski, J. Kijeňski, Appl. Catal. A 190 (2000) 87.
[15] M. Gliňski, J. Kijeňski, A. Jakubowski, Appl. Catal. A 128 (1995) 209.
[16] J. Stubenrauch, E. Brosha, J.M. Vohs, Catal. Today 28 (1996) 431.
[17] M. Gliňski, J. Kijeňski, React. Kinet. Catal. Lett. 69 (2000) 123.
[18] S.D. Randery, J.S. Warren, K.M. Dooley, Appl. Catal. A 226 (2002) 265.
[19] T.S. Hendren, K.M. Dooley, Catal. Today 85 (2003) 333.
[20] K. Parida, A. Samal, N.N. Das, Appl. Catal. A 166 (1998) 201.
[21] O. Nagashima, S. Sato, R. Takahashi, T. Sodesawa, J. Mol. Catal. A: Chem. 227 (2005) 231.
[22] W.A. Carvalho, P.B. Varaldo, M. Wallau, U. Schuchardt, Zeolites 18 (1997) 408. and references therein.
[23] S.C. Laha, P. Mukherjee, S.R. Sainkar, R. Kumar, J. Catal. 207 (2002) 213.
[24] A.S. Araujo, J.M.F.B. Aquino, M.J.B. Souza, A.O.S. Silva, J. Solid State Chem. 171 (2003) 371.
[25] M.D. Kadgaonkar, S.C. Laha, R.K. Pandey, P. Kumar, S.P. Mirajkar, R. Kumar, Catal. Today 97 (2004) 225.
[26] W. Yao, Y. Chen, L. Min, H. Fang, Z. Yan, H. Wang, J. Wang, J. Mol. Catal. A: Chem. 246 (2006) 162.
[27] K. M.S. Khalil, J. Colloid Interface Sci. 315 (2007) 562.
[28] Q. Zhao, Y. Xu, Y. Li, T. Jiang, C. Li, H. Yin, Appl. Surf. Sci. 255 (2009) 9425.
[29] J.B.M. Weckhuysen, D. Baetens, R. Schoonheydt, Angew. Chem. Int. Ed. 39 (2000) 3419.
[30] J. Li, Y. Hao, H. Li, M. Xia, X. Sun, L. Wang, Micro Meso. Mater. 120 (2009) 421.
[31] J.I.Di. Cosimo, C.R. Apesteguia, J. Catal. 116 (1989) 71.
[32] R. Larson, Acta Chem. Scand. 19 (1965) 783.
[33] P.T. Tanev, T.J. Pinnavaia, Science 267 (1995) 865.
[34] K.S.W. Sing, D.H. Everett, R.A.W. Haul, L. Mouscou, R.A. Pierotti, J. Rouquerol, T. Siemieniewska, Pure. Appl. Chem. 57 (1985) 603.
[35] A. Zukal, H. Sjiklová, J. Cjejka, Langmuir 24 (2008) 9837–9842.
[36] Ju. Xu, Wenhua. Zhang, Michael A. Morris, Justin D. Holmes, Mater. Chem. Phys. 104 (2007) 50–55.
[37] K.B. Sundaram, P. Wahid, Phys. Rev. B 161 (1990) 163.
[38] B.M. Reddy, S.C. Lcc, D.S. Han, S.E. Park, Appl. Catal. B: Environ. 87 (2009) 230.